chemosensors

Communication

Thermal Modulation of Resistance Gas Sensor Facilitates Recognition of Fragrance Odors

Ran Sui [1], Erpan Zhang [2,*], Xiaoshui Tang [3], Wenjun Yan [4,*], Yun Liu [5,*] and Houpan Zhou [4]

[1] School of HDU-ITMO Joint Institute, Hangzhou Dianzi University, Hangzhou 310018, China
[2] Institute of Advanced Magnetic Materials, College of Materials and Environmental Engineering, Hangzhou Dianzi University, Hangzhou 310018, China
[3] Jiangxi JCC East China Electrical New Material Technology Co., Ltd., Yingtan 335000, China
[4] School of Automation, Hangzhou Dianzi University, Hangzhou 310018, China
[5] School of Cyber Science and Engineering, Liaoning University, Shenyang 110036, China
* Correspondence: epzhang@hdu.edu.cn (E.Z.); yanwenjun@hdu.edu.cn (W.Y.); yunliu@lnu.edu.cn (Y.L.)

Abstract: Herein, we prepared two different MOS-based gas sensors with integrated micro-hotplates. The two sensors were employed to detect various fragrances (cedar, mandarin orange, rose A, and rose B), exhibiting similarly great sensing performances. The gas sensing properties of the MOS-based sensor depend on the sensor's operating temperature. In addition to isothermal operation, various pulse heating modes were applied to investigate the gas sensing performances with respect to the four fragrances. Multivariate gas sensing features of the four fragrances were obtained under different operating modes, which were utilized for the recognition of fragrance odors successfully, based on the long short-term memory (LSTM) algorithm.

Keywords: metal oxide; gas sensor; pulse heating; odor recognition

check for updates

Citation: Sui, R.; Zhang, E.; Tang, X.; Yan, W.; Liu, Y.; Zhou, H. Thermal Modulation of Resistance Gas Sensor Facilitates Recognition of Fragrance Odors. *Chemosensors* **2024**, *12*, 101. https://doi.org/10.3390/chemosensors12060101

Received: 24 April 2024
Revised: 2 June 2024
Accepted: 3 June 2024
Published: 5 June 2024

1. Introduction

In the pursuit of advancing olfactory sensing and fragrance quality assessment, it is paramount to acknowledge the importance of recognizing aromatic fragrances. Fragrances, with their dual cultural and economic significance, form an essential component of numerous products and environments. The accurate identification and thorough evaluation of these fragrances play a critical role in ensuring consumer satisfaction and safety [1].

In the past few decades, a variety of gas sensors, commonly referred to as electronic noses (e-noses), have been devised to replicate the human olfactory system. Through the analysis of odorant profiles across different compounds, these sensors demonstrate exceptional precision in assessing and identifying fragrances [2–4]. Within the spectrum of gas sensor technologies, such as optical [5,6], electrochemical [7,8], surface acoustic wave [9,10], microbalance [11], and metal oxide semiconductor (MOS) resistive types [12–14], MOS resistive sensors stand out especially for their low cost, compact size, and high sensitivity [14]. Their widespread application across environmental monitoring, food safety, and industrial production has positioned them as the cornerstone of e-nose technologies.

Meanwhile, computational methods such as pattern recognition [15], deep learning [16], and artificial neural networks [17] are crucial for interpreting e-nose data. These algorithms translate sensor signals into a range of recognizable odors. However, conventional e-noses often suffer from bulkiness and high power consumption due to the need for an extensive array of sensors to collect sufficient data for accurate gas identification.

Innovations in resistive gas sensors, which utilize metal oxide semiconductors as gas-sensitive materials, have revealed a close relationship between a sensor's response to gases and its operating temperature. Researchers have found that by adjusting the heating modes, such as through pulse heating modulation [18], a single sensor can generate

multiple sets of gas response signals. This innovation provides promise for reducing the abundance of sensors required in an e-nose system.

Expanding on this concept, the present work utilized isothermal and pulse heating modes to generate multiple distinctive datasets from a single sensor exposed to each analyte. A micro-array consisting of only two sensors was used, employing a sophisticated long short-term memory (LSTM) algorithm for the discrimination of the analyzed fragrance odors. The LSTM algorithm is specifically configured to process sequential data acquired from the dual-sensor system. Each sequence of data encapsulates a temporal profile of the sensors' responses to distinct fragrances. The LSTM network undergoes rigorous training to discern and learn patterns inherent in these data sequences. This capability enables the network to predict and categorize odor profiles with enhanced accuracy and precision [19]. This method not only enhances the practicality of e-nose systems in terms of size and energy consumption but also improves their ability to navigate the intricate scent profiles inherent to perfumery and scent-based industries, thus fulfilling the stringent requirements of perfumery and other industries reliant on precise scent detection.

2. Experimental Section

Materials and Characterization. The gas sensing materials utilized in this work were synthesized according to our previous report [20]. Briefly, 1 g as-received SnO_2 micro-powder with a diameter of ~3 μm (Zhitai Advanced Materials, Huzhou, China) was added to 800 μL ethanol. The mixture was ball-milled with a ball diameter of 1 mm for 4 h to create a uniform dispersion and nanoparticles. For one of the samples, 0.25 g tetraamminepalladium nitrate (Aladdin, Wuhan, China) was added to the synthesized dispersion as a palladium dopant. Finally, the nano-dispersions were annealed at 600 °C for 4 h in air with a heating rate of 2 °C/min. The obtained powders were taken as the gas sensing materials. A scanning electron microscope (SEM, FEI Nanosem 430) was used to characterize the morphology and microstructure of the synthesized materials. An energy-dispersive X-ray spectroscope (EDS) attached to the SEM was used to study the chemical composition. Powder X-ray diffraction (XRD) analyses were performed on a Bruker D8 Advance diffractometer with Cu Kα radiation (λ ≈ 1.54 Å).

Sensor fabrication. Sensors were prepared by integrating the sensing material onto commercial gold electrodes with an integrated micro-hotplate on a ceramic substrate, according to our previous work [21]. Briefly, 25 μL terpineol (Aladdin, China) was added to 5 mg of the obtained MOS powder with grinding for 20 min, and then one drop (~1 μL) was cast onto the parallel electrode area of the micro-hotplate (Figure 1a). The width of the gold electrode was 200 μm, and the separation distance between the parallel electrodes was ~180 μm. The heating temperature was controlled by the applied voltage of the micro-hotplate. Finally, the device was maintained at 300 °C by the hotplate for 3 days to promote the sensing layer deposition. The sensor based on SnO_2 was named s1, and the sensor based on Pd-SnO_2 was named s2. A micro-sensor array was prepared, consisting of sensors s1 and s2.

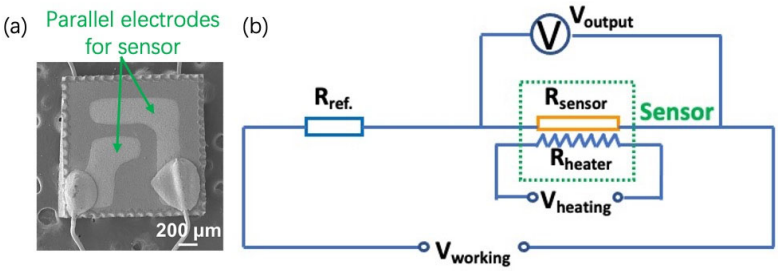

Figure 1. (**a**) An optical image of the micro-hotplate. (**b**) The working principle of the gas sensing measurement.

Gas sensing measurement. The gas sensing performances were investigated via a self-made system. For the gas sensing test, the sensor device was placed in a gas flow chamber (~10 cm^3). The analytes were pure essential oils of cedar, mandarin orange, and rose (Hangzhou Ziban, Hangzhou, China). The two kinds of rose essential oil, marked as rose A and rose B, were extracted from two different kinds of roses. The concentration of each analyte was controlled with mass flow controllers (MFCs) by the mixing ratio of the essential oil vapor generated by a VOC generator and pure dried air (Jingong, Jinjiang, China). The flow rate of the mixed gas to the test chamber was 300 cm^3/min. The heating modulation was controlled by a Keithley 2602B source-meter via applying different voltages to the heater formed on the backside of the sensor electrodes. To form a measurement circuit, a reference resistor ($R_{ref.}$) of 100 kW was connected in series, as illustrated in Figure 1b. By monitoring the voltage across R_{sensor}, the response of the sensor could be measured and collected by a data acquisition card (DAQ).

LSTM Algorithm for Data Interpretation in Gas Sensing. After data acquisition, the LSTM algorithm was utilized to process the sequential data collected from the sensors. This sophisticated computational technique is indispensable for deciphering the intricate temporal patterns of gas responses, enhancing the system's proficiency in distinguishing among various fragrances and concentrations. By exploiting LSTM's robust memory and learning capabilities, the algorithm acts as a potent tool for both predictive analysis and real-time detection. This advanced functionality significantly boosted the accuracy and reliability of the sensing system, as evidenced by the enhanced detection metrics compared to those of traditional methods.

3. Results and Discussion

3.1. Material Characteration

SEM images of the as-synthesized SnO_2 and Pd-SnO_2 nanoparticles are shown in Figure 2a,b. The SnO_2 and Pd-SnO_2 nanoparticles seem similarly homogeneous with a spherical shape at a diameter of ~20 nm. The doped Pd is not obvious in the sample Pd-SnO_2 nanoparticles. Moreover, the aggregation of nanoparticles is observed for both samples. The chemical composition of the Pd-SnO_2 sample is shown in Figure 2c, demonstrating the coexistence of Pd. The XRD patterns of the as-synthesized SnO_2 and Pd-SnO_2 nanoparticles are shown in Figure 2d. The XRD patterns agree well with the cassiterite structure of SnO_2 (JCPDS: 41-1445), without observed impurity phases and shifted peaks [22]. Due to the small amount of Pd, peaks associated with Pd are not observed in the XRD patterns.

3.2. Isothermal Response

Figure 3 presents the transient sensing curves of sensors s1 and s2 to various concentrations (volume concentration 5%–50%) of analytes (cedar, mandarin orange, rose A, and rose B) at 5 V of the microheater. The isothermal response is defined as Response = U_g/U_a, where U_g and U_a are the read-out voltage in an analyte and ambient air, respectively. Obviously, the voltage decreases upon exposure to each gaseous analyte and increases back to the original voltage after the analyte is off. Sample s1 exhibits a better linear response to 5%–50% analytes than sample s2. Furthermore, the response values of both sample s1 and s2 to cedar and mandarin orange are larger than those to rose A and rose B. For the MOS, oxygen molecules are initially adsorbed on the sensing layer and become ionized to chemisorbed O^- at the sensor's operating temperature of 300–400 °C [23,24]. Upon exposure to the tested fragrance molecules, which are volatile organics, the analyte molecules react with chemisorbed oxygen species O^-, releasing electrons back to the sensing layer to reduce the sensor resistance [23], which results in the voltage of the sensor decreasing. Due to the differences in the adsorption/desorption rates of different fragrance molecules on the sensing layers, the various response values were monitored [25].

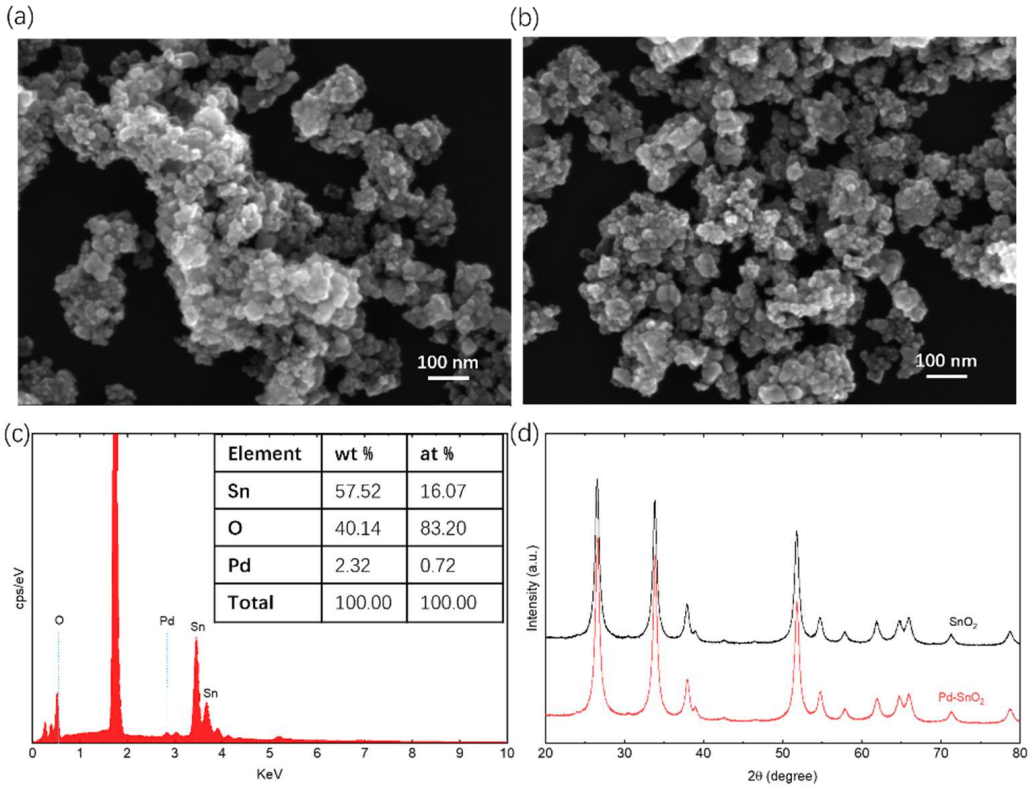

Figure 2. SEM images of (**a**) the as-synthesized SnO_2 nanoparticles and (**b**) Pd-SnO_2 nanoparticles. (**c**) EDS chemical analyses of the Pd-SnO_2 nanoparticles. (**d**) XRD patterns of the as-synthesized SnO_2 and Pd-SnO_2 nanoparticles.

3.3. Pulse Heating Response

The gas sensing performances of MOSs are mainly due to the redox reaction of analytes with chemisorbed oxygen on the sensing layer surface at the operating temperature of the sensor device. Thermally operating modes could generate a variety of gas sensing parameters, which have been reported [26,27]. Here, pulse heating voltage was applied to the micro-hotplate for thermal modulation. For the different pulse heating modes (PHMs), pulse-on (4 V/2 s) and pulse-off (5 V/2 s) was named PHM-1; pulse-on (4 V/2 s) and pulse-off (5 V/4 s) was named PHM-2; and pulse-on (4 V/4 s) and pulse-off (5 V/2 s) was named PHM-3. A pulse-on voltage of 5 V led to about 400 °C, and a pulse-off voltage of 4 V led to about 300 °C. During the whole gas sensing testing process, pulse on–off cycles were periodically repeated. The transient sensing curves under PHM-1 and the corresponding response vs. concentration curves to different analytes are presented in Figure 4. The resistance values of the sensing layer vary with different heating voltages, which correspond to different operating temperatures. Therefore, the sensor device generates two series of response values during the analyte sensing testing, that is, the response at a high voltage of 5 V named s1H and s2H and the response at a low voltage of 4 V named s1L and s2L. The two defined responses for sensor s1 are presented in the inset of Figure 4b. The response of sample s1 to cedar under PHM-1 is higher than that under isothermally operating mode, while the response of s1 to mandarin orange under PHM-1 is a little lower than the corresponding isothermal response.

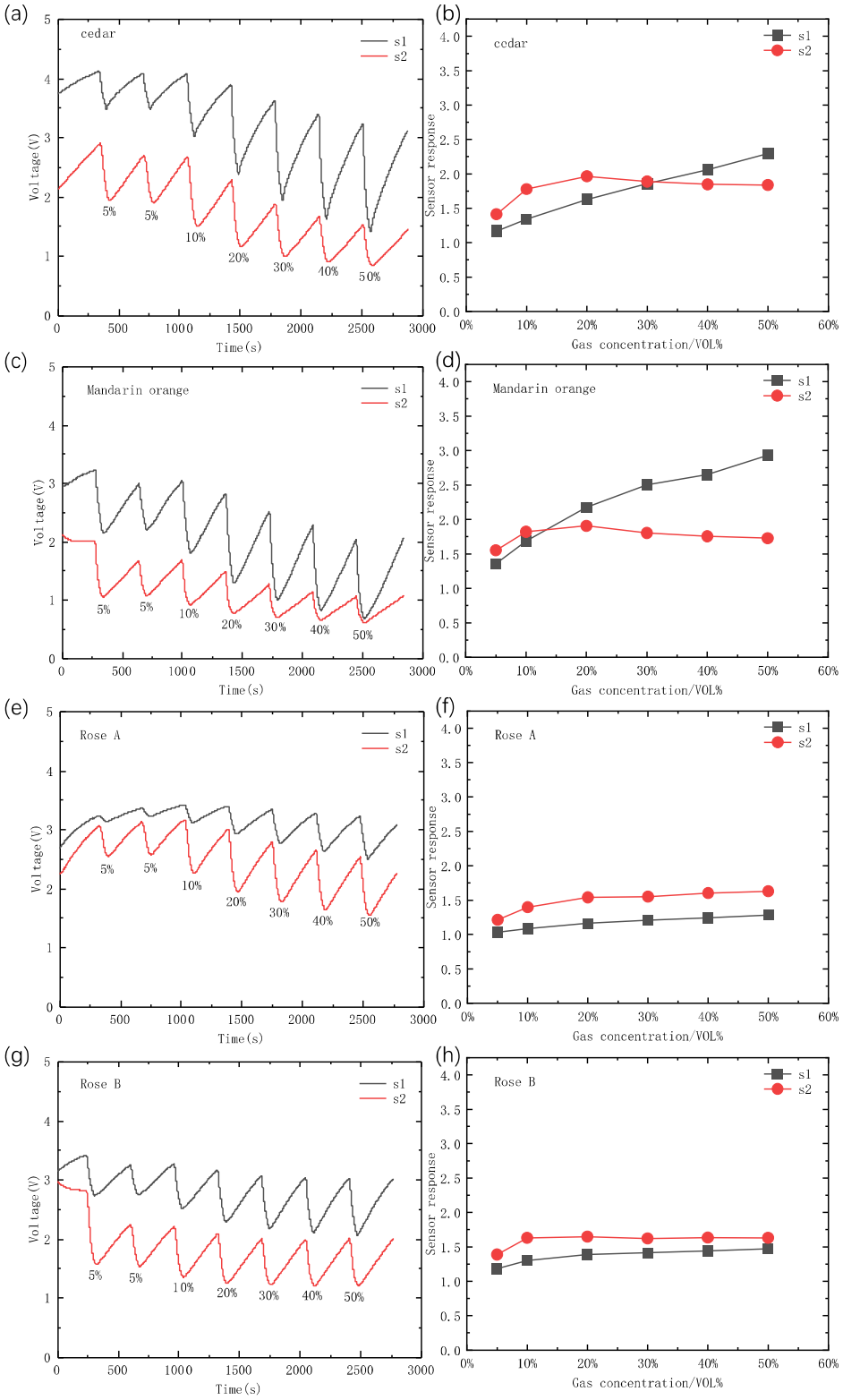

Figure 3. Isothermally transient sensing and the corresponding sensor response vs. concentration with the heater at 5 V: (**a**,**b**) cedar, (**c**,**d**) mandarin orange, (**e**,**f**) rose A, and (**g**,**h**) rose B. The response value is the average value of the response of 3 exposures to a given analyte concentration.

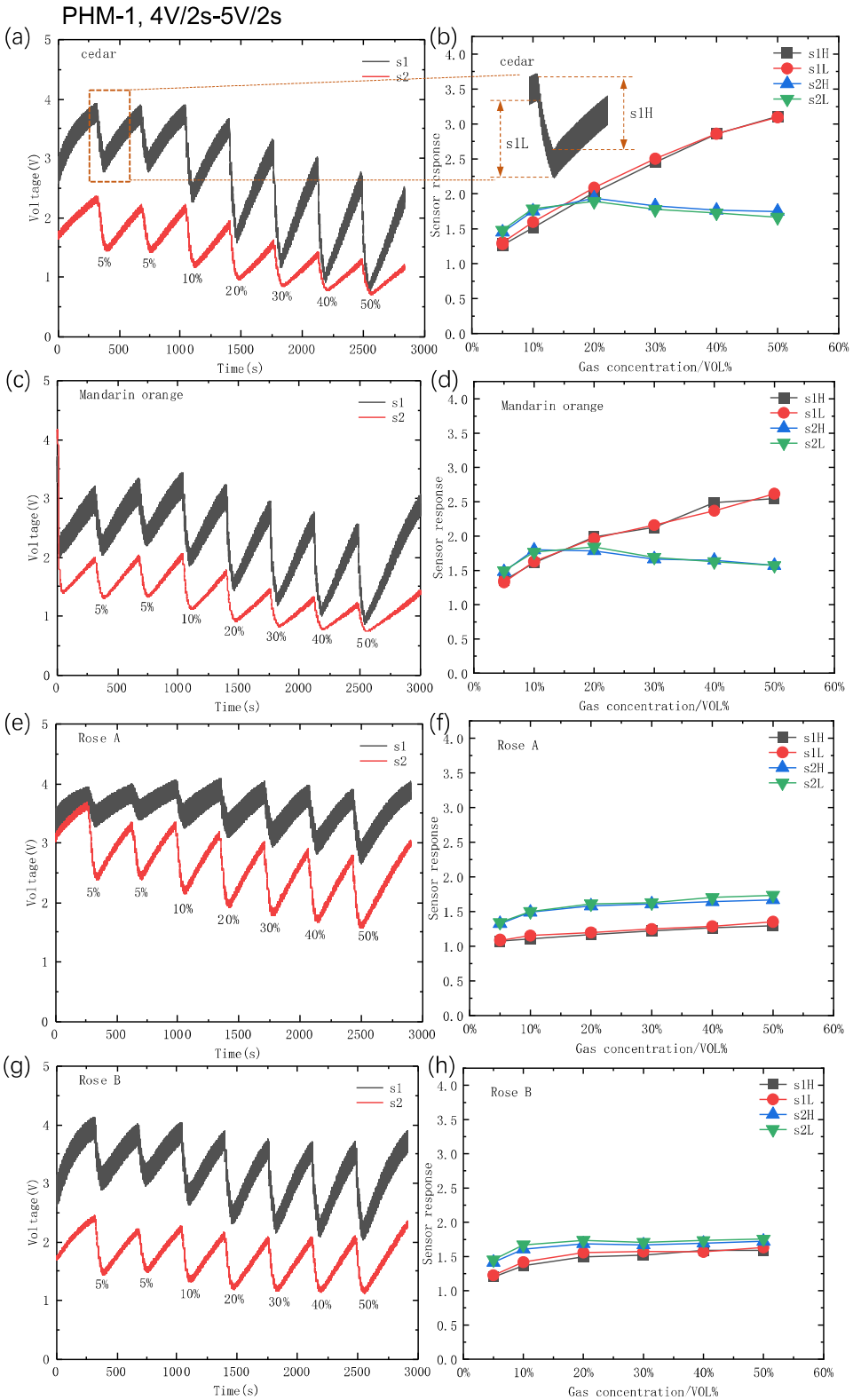

Figure 4. Transient sensing and the corresponding sensor response vs. concentration under PHM-1: (**a**,**b**) cedar, (**c**,**d**) mandarin orange, (**e**,**f**) rose A, and (**g**,**h**) rose B. The inset of (**b**) defined responses under the pulse heating mode. The response value is the average value of the response of 3 exposures to a given analyte concentration.

Transient sensing curves and the corresponding response vs. concentration to different analytes under PHM-2 and PHM-3 are presented in Figures 5 and 6, respectively. Obviously, under different operating modes, the gas sensing signals show slight differences, which could be utilized by artificial intelligence for fragrance odor recognition [25,28,29].

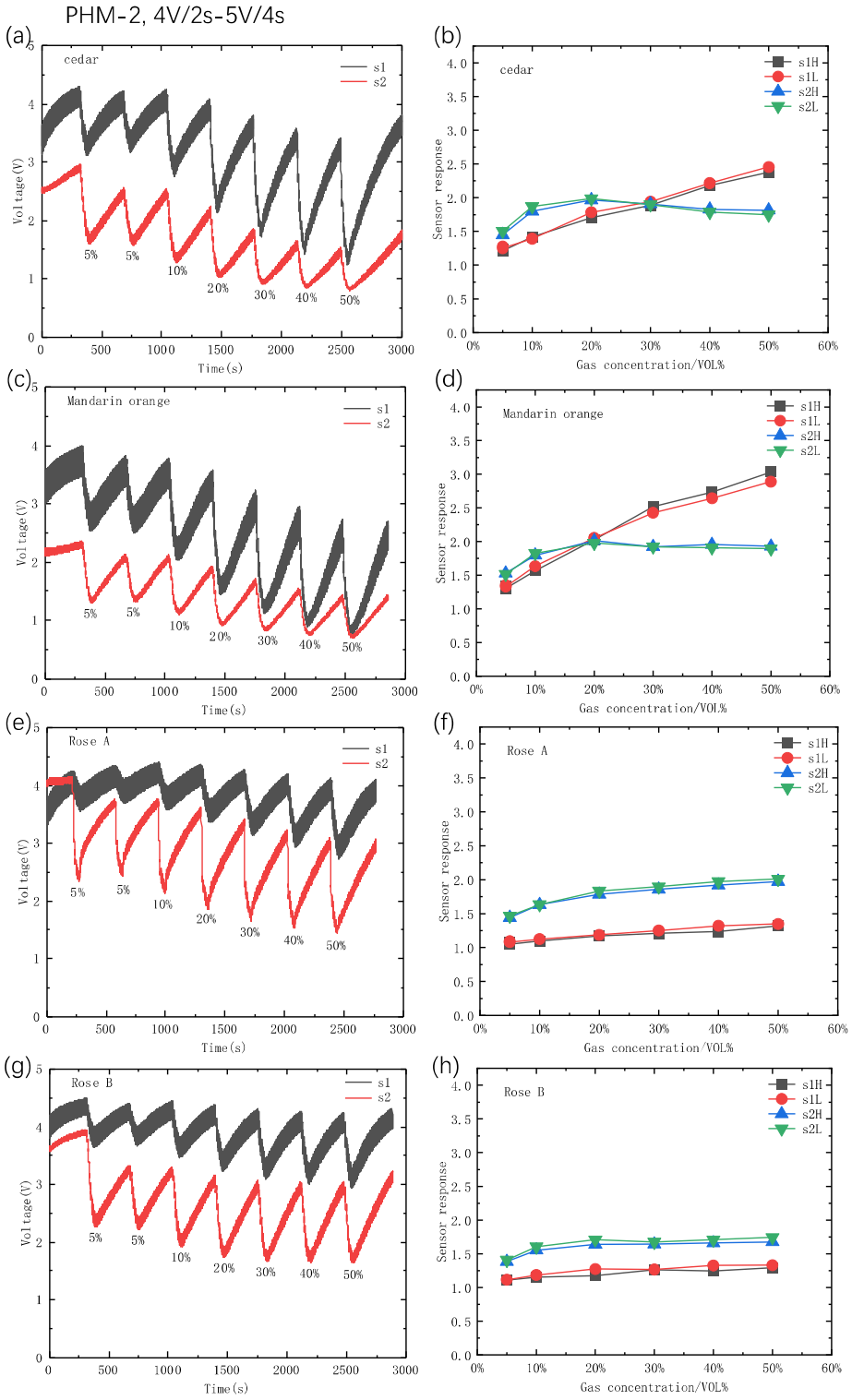

Figure 5. Transient sensing and the corresponding sensor response vs. concentration under PHM-2: (**a**,**b**) cedar, (**c**,**d**) mandarin orange, (**e**,**f**) rose A, and (**g**,**h**) rose B. The response value is the average value of the response of 3 exposures to a given analyte concentration.

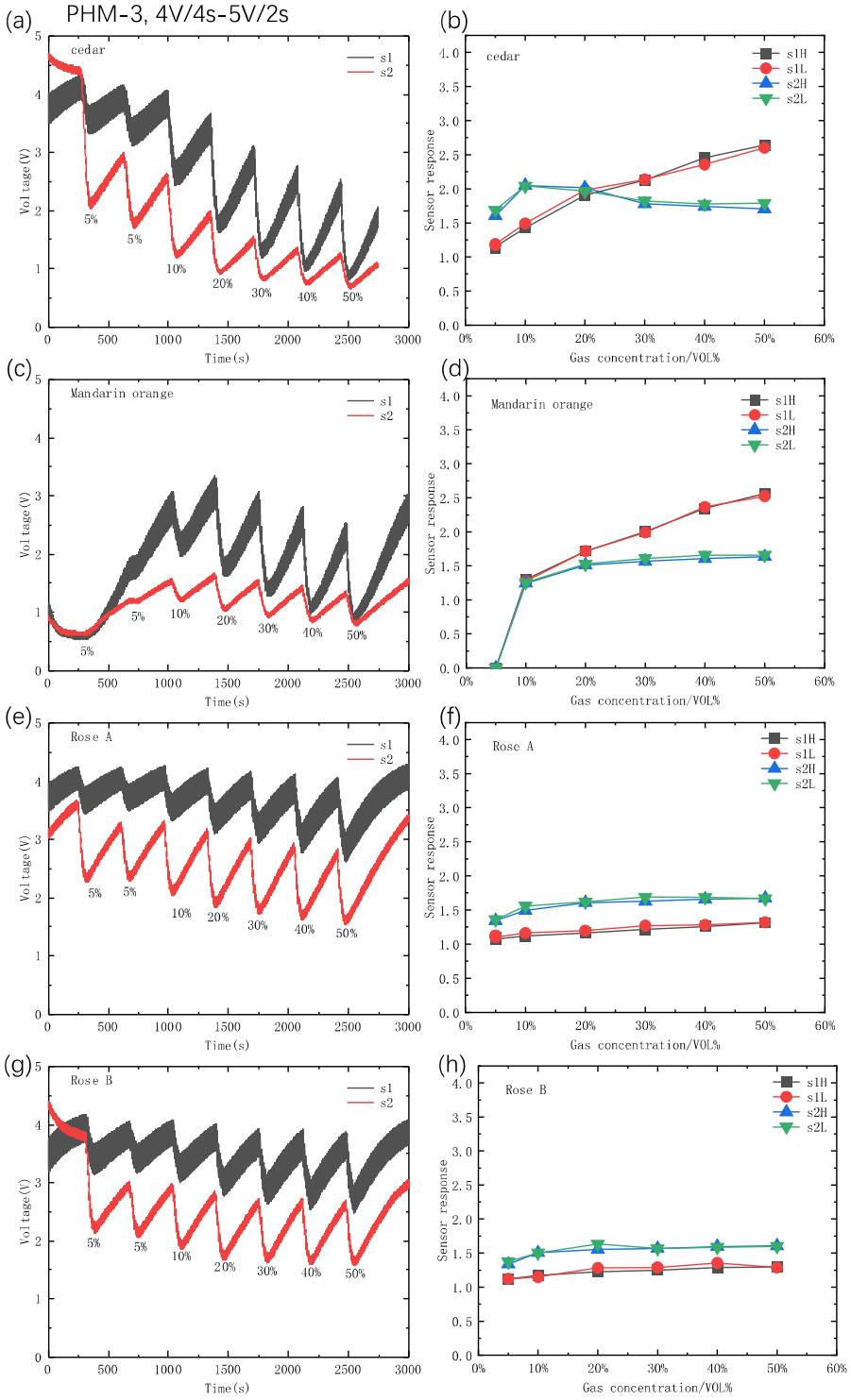

Figure 6. Transient sensing and the corresponding sensor response vs. concentration under PHM-3: (**a**,**b**) cedar, (**c**,**d**) mandarin orange, (**e**,**f**) rose A, and (**g**,**h**) rose B. The response value is the average value of the response of 3 exposures to a given analyte concentration.

According to the gas–MOS surface interaction, the gas sensing process is the relaxation of analyte and oxygen adsorption, as well as their redox, from nonequilibrium to equilibrium [28]. During the pulse heating cycles, the heating temperature changes periodically, and the adsorption and desorption of analyte vapor molecules on the sensing layer could be in a dynamic equilibrium. This results in relatively consistent response values at V_{min} and V_{max} under the pulse heating mode.

3.4. Odor Recognition

The architecture of the model consists of four one-dimensional convolutional layers, each followed by a rectified linear unit (ReLU) activation function, which is used for the non-linear transformation of the input data (as shown in Figure 7). Sequential data processing is facilitated by two LSTM layers designed to capture long-term dependencies. A dropout layer is included for regularization, reducing the potential for overfitting. The network concludes with a fully connected layer that consolidates features learned from previous layers, followed by a softmax layer that outputs the probability distribution across the defined classes.

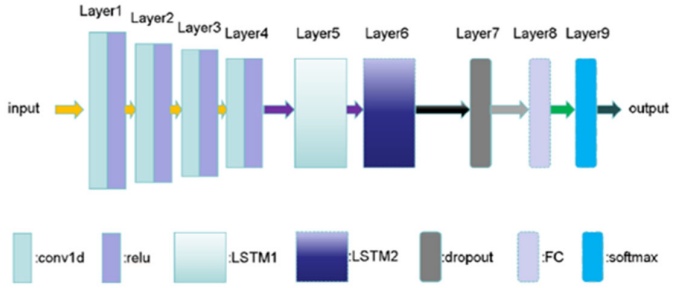

Figure 7. The architecture of the proposed LSTM algorithm.

For the odor recognition, Kalman filter was first employed on the raw sensing data to reduce noise, enhancing the data quality for further training machine learning models. Specific care should be taken to re-format time-series data properly for the easy construction of training model. Each input data should contain sufficient data points to reflect their underlying features and correlation. However, the traditional data segmentation will yield a relatively small size of input data.

Herein, we adopt the overlapping sliding-window technique to generate plenty of input data, fully taking advantage of the time-series data. The application of the sliding window technique resulted in a total of 18,485 samples after processing. Each sample in the processed datasets contains 1000 data points, obtained via a sliding window technique with a window size parameter set to 1000. With this, we produced all the time-series samples with 99% overlapping ratio specified.

To optimally prepare the data for model training and subsequent validation, the dataset was strategically partitioned into training and validation subsets. Specifically, 70% of the dataset was designated for training, enabling the model to extensively learn from the varied patterns present in the data. The remaining 30% was set aside for validation, which is crucial for evaluating the model's performance on new, unseen data and for reducing the risk of overfitting.

Different gases are denoted as distinct classes. Specifically, cedar is classified as Class 0, mandarin orange as Class 1, rose B as Class 2, and rose A as Class 3. We specified the number of time sequences for each input data, i.e., four, and thus, the dimension of each input sample was reshaped as $4 \times 25 \times 4$. Figure 8a depicts the evolution of the F1 score throughout the training epochs. The F1 score, which harmonizes precision and recall in its calculation, reaches a level close to 1 at a certain point, indicating the excellent performance of the model. Meanwhile, Figure 8b illustrates the reduction in the loss function value over the course of training. A lower loss indicates the better performance of the model on the training dataset, suggesting that the model is effectively learning from the data. Figure 8a represents the model's accuracy on the validation dataset. The accuracy shows a rapid improvement in the early stages of training and then plateaus, maintaining a high level, which reflects the model's ability to generalize well to unseen data. Figure 8b, analogous to the training loss, shows the model's loss on the validation dataset. Lower validation loss points towards a strong generalization capability of the model, signifying that it can perform well on data beyond the training set.

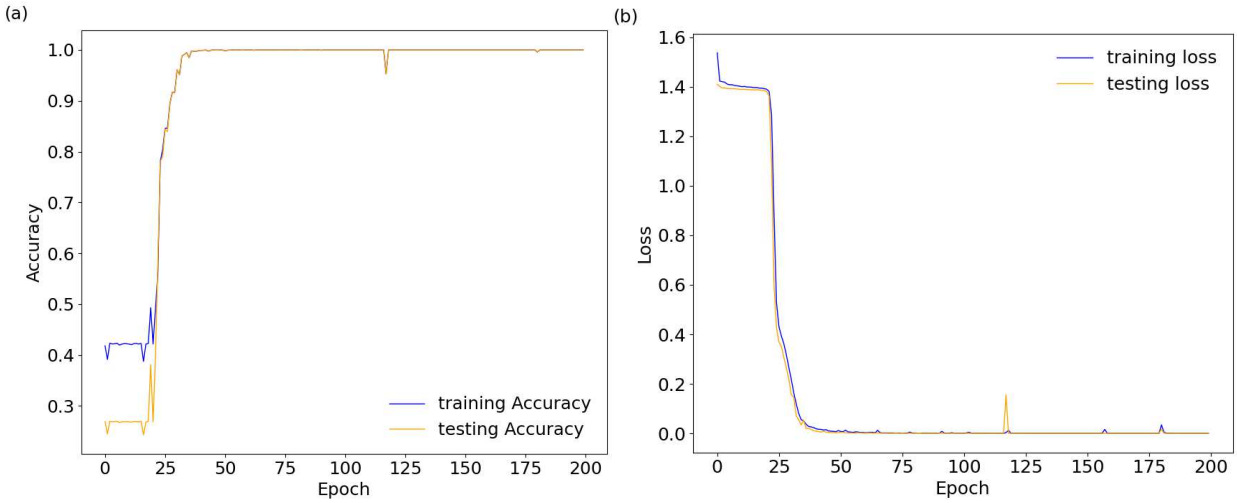

Figure 8. (**a**) Trend of training and testing accuracy. (**b**) Trend of training and testing loss.

To further visualize the classification results, Figure 9 depicts the confusion matrix to illustrate the classification performance of our model. Each row represents a gas in the actual class, while each column represents a gas in the predicted class. The diagonal elements of the matrix represent the number of correctly classified gases, while the off-diagonal elements indicate the misclassifications. This visualization provides valuable insights into the model's ability to distinguish different gas types. Each class is represented by a specific numeric label: 0 for cedar, 1 for mandarin orange, 2 for rose B, and 3 for rose A. Figure 9 indicates that our proposed model can realize the gases' discrimination correctly, with only a small number of misclassifications, demonstrating the effectiveness of our model in gas recognition. The accuracy was calculated to be 91.2%, denoting a high level of model precision in classification. In addition, we calculated the classification metrics such as the accuracy, recall, F1 score, true positive rate (TPR), and false positive rate (FPR) [30,31], which were 95.6%, 91.2%, 91.2%, 91.2%, and 2.9%, respectively. The results further demonstrated the good performance of the proposed model in the present fragrance odor classification.

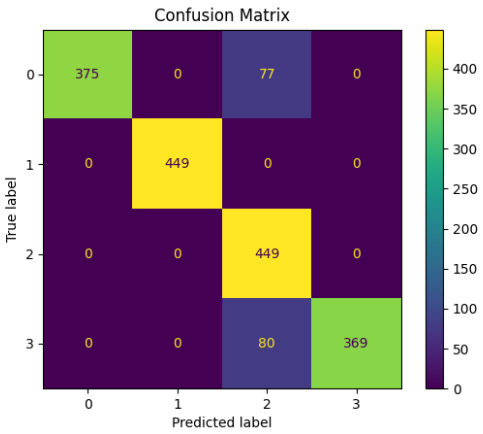

Figure 9. Classification result based on confusion matrix.

4. Conclusions

Herein, we prepared two different MOS-based gas sensors integrating a micro-hotplate. Isothermal operating and three kinds of pulse heating modes (pulse-on 4 V/2 s and pulse-off 5 V/2 s, pulse-on 4 V/2 s and pulse-off 5 V/4 s, and pulse-on 4 V/4 s and pulse-off 5 V/2 s) were applied to investigate the gas sensing performances on four fragrances (cedar, mandarin orange, rose A, and rose B). As the gas sensing performances of MOS-based sensors depend on the sensors' operating temperature, the two presented samples exhibited

multivariable transient sensing signals to different analytes. Via the LSTM algorithm, we realized the efficient and intelligent discrimination of cedar, mandarin orange, rose A, and rose B. This work provides insight for the further development of intelligent odor recognition based on micro-sensor arrays.

Author Contributions: R.S.: Methodology, Validation, Original draft. E.Z.: Conceptualization, Investigation, Methodology, Writing—review and editing. X.T.: Investigation, Formal analysis. W.Y.: Writing—original draft, Methodology, Conceptualization. Y.L.: Methodology, Writing—review and editing. H.Z.: Resources, Conceptualization, Supervision. All authors have read and agreed to the published version of the manuscript.

Funding: This work is supported by the National Natural Science Foundation of China (No. 62201185, 52377022), Liaoning Province Natural Science Foundation (Grant 2023-MS-139), and Shenyang science and technology plan project (Grant 23-407-3-32). W.Y. acknowledges the 2011 Zhejiang Regional Collaborative Innovation Centre for Smart City.

Data Availability Statement: Data are contained within the article.

Conflicts of Interest: The authors declare no competing financial interests. Readers are welcome to comment on the online version of this paper.

References

1. Jarboui, A. Application of Electrochemical Sensors as an Alternative Tool for Perfume Evaluation. Master's Thesis, Polytechnic Institute of Bragança, Bragança, Portugal, 2019.
2. Chen, H.; Huo, D.; Zhang, J. Gas Recognition in E-Nose System: A Review. *IEEE Trans. Biomed. Circuits Syst.* **2022**, *16*, 169–184. [CrossRef] [PubMed]
3. Branca, A.; Simonian, P.; Ferrante, M.; Novas, E.; Negri, R.M. Electronic nose based discrimination of a perfumery compound in a fragrance. *Sens. Actuators B Chem.* **2003**, *92*, 222–227. [CrossRef]
4. James, D.; Scott, S.; Ali, Z.; O'Hare, W.T. Chemical sensors for electronic nose systems. *Microchim. Acta* **2005**, *149*, 1–17. [CrossRef]
5. Paliwal, A.; Sharma, A.; Tomar, M.; Gupta, V. Carbon monoxide (CO) optical gas sensor based on ZnO thin films. *Sens. Actuators B-Chem.* **2017**, *250*, 679–685. [CrossRef]
6. Zhang, Y.-N.; Zhao, Y.; Bai, L.; Zhang, F. High-Sensitivity Optical Fiber Gas Sensors Based on Novel Optical Devices. *Instrum. Sci. Technol.* **2013**, *41*, 187–201. [CrossRef]
7. Li, H.; Mu, X.; Yang, Y.; Mason, A.J. Low Power Multimode Electrochemical Gas Sensor Array System for Wearable Health and Safety Monitoring. *IEEE Sens. J.* **2014**, *14*, 3391–3399. [CrossRef]
8. Wan, H.; Yin, H.; Lin, L.; Zeng, X.; Mason, A.J. Miniaturized planar room temperature ionic liquid electrochemical gas sensor for rapid multiple gas pollutants monitoring. *Sens. Actuators B-Chem.* **2018**, *255*, 638–646. [CrossRef]
9. Jakubik, W.P. Surface acoustic wave-based gas sensors. *Thin Solid Film.* **2011**, *520*, 986–993. [CrossRef]
10. Gao, F.; Boussaid, F.; Xuan, W.; Tsui, C.-Y.; Bermak, A. Dual Transduction Surface Acoustic Wave Gas Sensor for VOC Discrimination. *IEEE Electron Device Lett.* **2018**, *39*, 1920–1923. [CrossRef]
11. Compagnone, D.; Faieta, M.; Pizzoni, D.; Di Natale, C.; Paolesse, R.; Van Caelenberg, T.; Beheydt, B.; Pittia, P. Quartz crystal microbalance gas sensor arrays for the quality control of chocolate. *Sens. Actuators B-Chem.* **2015**, *207*, 1114–1120. [CrossRef]
12. Hua, Z.; Li, Y.; Zeng, Y.; Wu, Y. A theoretical investigation of the power-law response of metal oxide semiconductor gas sensors I: Schottky barrier control. *Sens. Actuators B-Chem.* **2018**, *255*, 1911–1919. [CrossRef]
13. Schultealbert, C.; Baur, T.; Schütze, A.; Böttcher, S.; Sauerwald, T. A novel approach towards calibrated measurement of trace gases using metal oxide semiconductor sensors. *Sens. Actuators B-Chem.* **2017**, *239*, 390–396. [CrossRef]
14. Wu, R.; Tian, L.; Li, H.; Liu, H.; Luo, J.; Tian, X.; Hua, Z.; Wu, Y.; Fan, S. A selective methane gas sensor based on metal oxide semiconductor equipped with an on-chip microfilter. *Sens. Actuators B-Chem.* **2022**, *359*, 131557. [CrossRef]
15. Kuske, M.; Padilla, M.; Romain, A.C.; Nicolas, J.; Rubio, R.; Marco, S. Detection of diverse mould species growing on building materials by gas sensor arrays and pattern recognition. *Sens. Actuators B-Chem.* **2006**, *119*, 33–40. [CrossRef]
16. Badawi, D.; Bassi, I.; Ozev, S.; Enis, A. Cetin Deep-Learning-Based Gas Leak Source Localization From Sparse Sensor Data. *IEEE Sens. J.* **2022**, *22*, 20999–21008. [CrossRef]
17. Palme, T.; Fast, M.; Thern, M. Gas turbine sensor validation through classification with artificial neural networks. *Appl. Energy* **2011**, *88*, 3898–3904. [CrossRef]
18. Hu, Y.; Tian, Y.; Zhuang, Y.; Zhao, C.; Wang, F. Rapid Gas Sensing Based on Pulse Heating and Deep Learning. In Proceedings of the 2021 IEEE 34th International Conference on Micro Electro Mechanical Systems (MEMS), Gainesville, FL, USA, 25–29 January 2021; pp. 438–441.
19. Greff, K.; Srivastava, R.K.; Koutník, J.; Steunebrink, B.R.; Schmidhuber, J. LSTM: A Search Space Odyssey. *IEEE Trans. Neural Netw. Learn. Syst.* **2017**, *28*, 2222–2232. [CrossRef]

20. Chen, Y.; Li, M.; Yan, W.; Zhuang, X.; Ng, K.W.; Cheng, X. Sensitive and low-power metal oxide gas sensors with a low-cost microelectromechanical heater. *ACS Omega* **2021**, *6*, 1216–1222. [CrossRef] [PubMed]
21. Zhou, S.; Yan, W.; Ling, M.; Liang, C. High-response H_2 sensing performances of ZnO nanosheets modulated by oxygen vacancies. *Inorg. Chem. Front.* **2023**, *10*, 3255–3262. [CrossRef]
22. Suematsu, K.; Sasaki, M.; Ma, N.; Yuasa, M.; Shimanoe, K. Antimony-doped tin dioxide gas sensors exhibiting high stability in the sensitivity to humidity changes. *ACS Sens.* **2016**, *1*, 913–920. [CrossRef]
23. Yan, W.; Chen, Y.; Zeng, X.; Wu, G.; Jiang, W.; Wei, D.; Ling, M.; Ng, K.W.; Qin, Y. Ultrasensitive ethanol sensor based on segregated ZnO-In_2O_3 porous nanosheets. *Appl. Surf. Sci.* **2021**, *535*, 147697. [CrossRef]
24. Yan, W.; Xu, H.; Ling, M.; Zhou, S.; Qiu, T.; Deng, Y.; Zhao, Z.; Zhang, E. MOF-derived porous hollow Co_3O_4@ ZnO cages for high-performance MEMS trimethylamine sensors. *ACS Sens.* **2021**, *6*, 2613–2621. [CrossRef] [PubMed]
25. Acharyya, S.; Nag, S.; Kimbahune, S.; Ghose, A.; Pal, A.; Guha, P.K. Selective Discrimination of VOCs Applying Gas Sensing Kinetic Analysis over a Metal Oxide-Based Chemiresistive Gas Sensor. *Acs Sens.* **2021**, *6*, 2218–2224. [CrossRef] [PubMed]
26. Yan, W.; Luo, W.; Li, J.; Li, M. Highly Selective MEMS Gas Sensor to Detect H_2 and NH_3 with Tunable Discrimination. *IEEE Sens. J.* **2024**, *24*, 7473–7481. [CrossRef]
27. Suematsu, K.; Harano, W.; Oyama, T.; Shin, Y.; Watanabe, K.; Shimanoe, K. Pulse-driven semiconductor gas sensors toward ppt level toluene detection. *Anal. Chem.* **2018**, *90*, 11219–11223. [CrossRef] [PubMed]
28. Tang, W.; Chen, Z.; Song, Z.; Wang, C.; Wan, Z.A.; Chan, C.L.J.; Chen, Z.; Ye, W.; Fan, Z. Microheater integrated nanotube array gas sensor for parts-per-trillion level gas detection and single sensor-based gas discrimination. *ACS Nano* **2022**, *16*, 10968–10978. [CrossRef] [PubMed]
29. Kang, M.; Cho, I.; Park, J.; Jeong, J.; Lee, K.; Lee, B.; Del Orbe Henriquez, D.; Yoon, K.; Park, I. High accuracy real-time multi-gas identification by a batch-uniform gas sensor array and deep learning algorithm. *ACS Sens.* **2022**, *7*, 430–440. [CrossRef]
30. Muhuri, P.S.; Chatterjee, P.; Yuan, X.; Roy, K.; Esterline, A. Using a long short-term memory recurrent neural network (LSTM-RNN) to classify network attacks. *Information* **2020**, *11*, 243. [CrossRef]
31. Mekruksavanich, S.; Jitpattanakul, A. Lstm networks using smartphone data for sensor-based human activity recognition in smart homes. *Sensors* **2021**, *21*, 1636. [CrossRef]